

1 **Large amplitude internal tides, solitary waves and**
2 **turbulence in the central Bay of Biscay**

3 X. H. Xie^{1*}, Y. Cuypers¹, P. Bouruet-Aubertot¹, B. Ferron²
4 A. Pichon³, A. Lourenço¹, N. Cortes²

5 ¹LOCEAN, UMR7167, Université Pierre et Marie Curie, 75252 Paris, France.

6 ²LPO, Ifremer, UMR 6523 CNRS-IFREMER-IRD-UBO,Plouzané, 29280 Brest, France

7 ³SHOM, Centre Militaire d'Océanographie, 29603 Brest, France

8 **Abstract**

9 Microstructure and fine-scale measurements collected in the central Bay of Biscay
10 during MOUTON experiment are analyzed to investigate the dynamics of internal
11 waves and associated mixing. Large amplitude internal tides (ITs), that excite internal
12 solitary waves (ISWs) in the thermocline, are observed. ITs are dominated by modes
13 3 and 4, while ISWs projects on mode-1 that is trapped in the thermocline. Therein,
14 ITs generate a persistent narrow shear band, which is strongly correlated with the
15 enhanced dissipation rate in the thermocline. This strong dissipation rate is further
16 reinforced in presence of ISWs. Dissipation rates during the period without ISWs
17 largely agree with the MacKinnon-Gregg scaling proposed for internal wave fields
18 dominated by a low frequency mode. On the opposite, they show poor agreement with
19 the Gregg-Henyey parameterization valid for internal wave fields close to the GM
20 model. The agreement with the MacKinnon-Gregg scaling is consistent with the fact
21 that turbulent mixing is here driven by the low-frequency internal tidal shear.

22
23 *Email: xiaohuihh_2006@yahoo.com.cn

26 1. Introduction

27 It is well known that the Bay of Biscay (BB) is a marginal sea with large
28 amplitude internal tides (ITs). Therein, ITs are mainly generated on the slope via
29 interaction between the barotropic tide and the steep topography [e.g. *Pingree and*
30 *New, 1991; Gerkema et al., 2004; Pichon et al., 2011*]. Once generated, they
31 propagate both seaward and shoreward. Linear internal-wave theory and
32 observations show that the seaward traveling ITs propagate along a beam or ray path
33 with a slope to the horizontal given by:

$$34 \quad c = \pm [(\omega^2 - f^2)/(N^2 - \omega^2)]^{1/2}, \quad (1)$$

35 where ω is the semidiurnal frequency, f is the local inertial frequency and N is the
36 buoyancy frequency [*Pingree and New, 1991*]. The theory also predicts that the
37 offshore propagating beam first reflects at the bottom and next at the sea surface in
38 the central BB [*Gerkema et al., 2004; Pichon et al., 2011*] (Fig.1.a). Using
39 temperature and velocity records obtained from the central BB, *New and Pingree*
40 [1990] observed large internal interfacial tides and internal solitary waves (ISWs) in
41 the thermocline. These waves were as large as those observed at the shelf edge, and
42 they were thus conjectured to be locally aroused in the central BB, where internal
43 tidal beams hit the seasonal thermocline near the sea surface. This hypothesis was
44 confirmed by satellite imagery [*New and Da Silva, 2002*]. Theoretical framework for
45 this process was given by *Gerkema* (2001) (hereafter referred as to G01) who showed
46 that scattering of IT beams in the thermocline leads to the local generation of large
47 ITs and ISWs. This scenario was retrieved in other numerical models [*Grisouard et al,*
48 2011] and reproduced in laboratory experiments [*Mercier et al, 2012*].

49 While there are numerous insights on ITs and ISWs in the BB, there have never
50 been measurements in the BB allowing a fine characterization of ITs and ISWs.

51 Another aspect that has never been quantified is the turbulent mixing induced by these
52 internal waves. In this paper, we report on joint fine-scale and microstructure
53 measurements performed for the first time in the central BB. We first characterize
54 vertical structures of ITs and ISWs and next dissipation rate (ϵ) of turbulent kinetic
55 energy and turbulent mixing induced by ITs and ISWs. Eventually, fine-scale
56 parameterizations are tested against microstructure measurements.

57

58 **2. Data**

59 Data were collected at a location (45.75°N, 7.38°W) in the central BB during the
60 MOUTON experiment in summer 2008, where the water depth is about 4800 m (Fig.
61 1a). This location is about 200 km away from generation area of internal tidal beams
62 on the northern slope of BB (Fig. 1a) [Pichon *et al.*, 2011]. From Sept.18th,
63 01(h):10(min) until Sept. 19th, 04:00, combined CTD/LADCP yo-yoing was
64 performed. Sixteen profiles were collected with an effective depth range from 6 to
65 2663 m. From 04:50 to 21:20 on Sept.19th, two microstructure instruments, VMP
66 (Vertical Microstructure Profiler) and SCAMP (Self-Contained Autonomous
67 Microstructure Profiler), were alternatively deployed. Dissipation rate estimates with
68 Scamp are based on Batchelor fitting of the temperature gradient spectrum measured
69 by high frequency temperature sensors [Ruddick *et al.*, 2000], whereas VMP estimates
70 are based on measurements of microscale vertical shear. While 19 VMP profiles were
71 obtained from the surface to depths of 400-500 m, 15 Scamp profiles were collected
72 from the surface to depths of 70-110 m. Data above 10 m were removed due to the
73 contamination by the ship's wake. Current velocities were inferred from two 150-kHz
74 and 38-kHz broadband shipboard ADCPs. Measurement range of the former ADCP is
75 from 18 m to 162 m with a 2-min time-average interval and 4-m bin, while that of the

76 latter is from 55 m to 1231 m with the same time-average interval and 24-m bin. We
77 used here the 150-kHz ADCP data to compute 4-m shear (S_4) during microstructure
78 measurements.

79 CTD data were de-spiked and averaged into 1-m bins, while ε is computed from
80 VMP and Scamp data using 1m bins. Since Scamp was not equipped with
81 conductivity sensors, salinity during Scamp measurements was estimated by a linear
82 interpolation of VMP salinity data.

83

84 **3. Results**

85 **3.1 Mean stratification and semidiurnal IT ray path**

86 The time-averaged CTD data were used to compute the buoyancy frequency $N(z)$.
87 The climatological temperature and salinity data at the measurement location obtained
88 from the *World Ocean Atlas* 2009 were used to complete the profile below 2663 m
89 depth (Fig. 1b). The $N(z)$ profile showing the largest value at 40-70 m (seasonal
90 thermocline) and a small peak near 800 m (permanent pycnocline) (Fig. 1b) is typical
91 for the central BB during summer [G01]. An internal tidal beam path is computed
92 using $N(z)$ and a typical model topography in the BB. The surface reflection site of
93 internal tidal beams in the central BB is ~140 km away from their generation location
94 and ~60 km away from our observation site (Fig. 1a, embedded panel).

95 **3.2 Internal interfacial tides and ISWs**

96 Time series of temperature show large thermocline depressions with a semidiurnal
97 period, so called as internal interfacial tides (Fig. 2a). Their amplitude from crest to
98 trough is in the range 40-70 m. Note that the largest isotherm displacements are often
99 observed below 1800 m (not shown). These large displacements are likely induced by
100 the descending beam, which intersects the mooring position at large depth (see

101 inserted panel in Fig. 1a). During the second observation period, that of
102 VMP/SCAMP measurements, the isotherms slope in the thermocline depressions
103 become steeper, implying the enhancement of IT nonlinearity. As a result, high-
104 frequency ISWs are generated in troughs and surface velocities are increased (Figs. 2b
105 and 3a). Note that the averaged time interval between two ISWs events is equal to 25-
106 min, therefore ISWs could not be identified from temperature data due to their low
107 temporal resolution (about 20-min) but only from ADCP data.

108 We determine in the following the directions of propagation of ITs and ISWs as
109 well as their vertical structure. The large thermocline depressions often cause
110 southward velocity in the surface layer (Figs. 2c and 2d), implying a southward
111 propagation of ITs. These large southward interfacial tides likely result from the
112 scattering of the seaward traveling internal tidal beams generated on the northern
113 slope [G01]. However, a more complex pattern can be observed on Sept.19th, 6h-12h.
114 During this period, two oppositely travelling troughs are observed in the large
115 thermocline depression: the first one generates southward surface velocity while the
116 second one induces northward surface velocity. The trough propagating northward
117 may be associated with internal tidal beams originating from the southern slope
118 [Pichon *et al.*, 2011]. Since the velocity direction caused by ISWs is the same as that
119 of thermocline depressions (Fig. 2c), their propagating direction is consistent with that
120 of internal tides.

121 To investigate the vertical structure of ITs and ISWs, we have computed vertical
122 modal functions of displacement $\Phi(z)$ and horizontal velocity $\Pi(z)$ at semidiurnal and
123 $1/25 \text{ min}^{-1}$ frequencies following equations 6.10.2, 6.10.3 and 6.10.6 from Gill [1982].
124 Modal structures of waves with these two frequencies show large difference (Figs. 1c
125 and 1d), as the high frequency is larger than N below the thermocline (see Fig. 1b). As

126 a result, the high-frequency modes are trapped in the thermocline (Figs. 1d and 2b).
127 To distinguish mode functions of high-frequency waves from that of low-frequency
128 waves, we refer to the former as trapped mode structures and to the latter as IT mode
129 thereafter. In order to infer IT mode structures, we compute time series of isopycnal
130 vertical displacement from CTD measurements. Then we extract the semidiurnal
131 amplitude for each depth using a harmonic analysis of the displacement time series.
132 The resulting normalized displacement profile at the semidiurnal frequency is plotted
133 in Figure 1c. The mode-3 structure roughly reflects depth variation of IT displacement
134 except for depths below 1800 m (Fig. 1g), where more modes may be present due to
135 the downward IT beam. A mode projection on IT displacements by the least square
136 method indicates that mode-3 (mode-4) explains about 61% (23%) of total potential
137 energy above the depth of 500 m. Accordingly, the sum of the projected mode-3 and
138 mode-4 reproduces well the variation of semidiurnal displacement above 500 m depth
139 (Fig. 1c). Meanwhile, measured velocity profiles when ISWs pass the fixed point are
140 well fitted by trapped mode-1 (Fig. 1i). Note that as vertical advection of velocity
141 signals by thermocline displacements is strong (see Fig. 2c), Eulerian depth of
142 velocity profiles in Figures 1h and 1i was transformed to semi-Lagrangian depth.
143 Interestingly, the vertical structures of IT mode-4 and trapped mode-1 are very similar
144 within the thermocline (Fig. 1e), which suggests that the observed ISWs are likely to
145 result from mode-4 ITs.

146 **3.3 Microstructure measurements**

147 Time series of dissipation rates is shown in Figure 3b. The largest ε values often
148 occur near the surface, which may be directly associated with wind stirring in the
149 mixed layer. Enhanced ε values are also encountered in the thermocline with a mean ε
150 value of $2.3 \times 10^{-8} \text{ Wkg}^{-1}$. Diapycnal diffusivity, K_p , was computed according to the

151 relationship established by *Shih et al.* (2005) who distinguished different regimes as a
152 function of turbulent intensity: $K_p = \lambda \varepsilon / N^2$, where $\lambda = 2[\varepsilon / (vN^2)]^{-1/2}$ (v is the molecular
153 viscosity) when $\varepsilon / (vN^2) > 100$ otherwise $\lambda = 0.2$. Enhanced K_p , also occur in the
154 thermocline (Fig. 3c) with a mean value equal to $1.5 \times 10^{-5} \text{m}^2 \text{s}^{-1}$, slightly larger than
155 background values found in the open ocean thermocline. Below the thermocline,
156 mixing becomes quite weak ($\varepsilon < 10^{-9} \text{WKg}^{-1}$, $K_p < 10^{-5} \text{m}^2 \text{s}^{-1}$) except for a few patches.
157 The time-mean profiles along isotherms also display the above depth variations of ε
158 and K_p (inserted panels in Figs. 3b and 3c).

159 In the 4-m shear field, a narrow band of strong shear caused by ITs is clearly
160 identified within the thermocline with the strongest stratification (Fig. 3e). Because of
161 the large thermocline displacement caused by interfacial tides, the strong shear band
162 is vertically elevated and depressed in a semidiurnal period. The time-averaged S^2 and
163 N^2 show the same variation with decreasing temperature/depth (inserted panel in Fig.
164 3d). However, S^2 is smaller than N^2 , implying that the Richardson number Ri ($= N^2 / S^2$)
165 is larger than 1 and that the large-scale waves are stable toward shear instability.
166 Since the strong stratification in the top of the thermocline (Fig. 3d) inhibits the
167 penetration of surface turbulence into the thermocline, the enhanced ε inside the
168 thermocline is likely to be associated with strong shears in the thermocline (Fig. 3e).
169 Below the thermocline, weaker ε is associated with smaller shear and stratification. In
170 addition, dissipation rates as well as K_p in the troughs are elevated relative to those in
171 the crests. This may be associated with disintegration of IT troughs into a group of
172 ISWs that further enhances turbulent mixing.

173 **3.4 Mixing Parameterization**

174 In order to investigate further the relationship between dissipation rates and
175 shear/stratification, the observed dissipation rates were averaged into logarithmic bins

176 of N^2 and S^2 . Two parameterizations, MacKinnon-Gregg (M-G) and Gregg-Henyey
 177 (G-H), are tested. The former was found to be relevant in situations where shear of
 178 large-scale waves and energy of small-scale waves do not maintain a particular
 179 relationship through the Garrett-Munk (GM) spectrum as illustrated for internal wave
 180 mixing in the coastal ocean [*MacKinnon and Gregg, 2003*], while the latter applies
 181 for internal wave fields with the GM spectral shape and is widely encountered in the
 182 open ocean [*Gregg, 1989*]. These two parameterizations are given by

$$183 \quad \varepsilon_{GH} = 1.8 \times 10^{-6} f \cosh^{-1}(N_0/f) (S/S_{GM})^4 (N/N_0)^2$$

$$184 \quad S_{GM}^4 = 1.6 \times 10^{-10} (N/N_0)^2 \quad (2)$$

185 and

$$186 \quad \varepsilon_{MG} = \varepsilon_0 (N/N_0)(S/S_0), \quad (3)$$

187 where $N_0 = S_0 = 0.0052 \text{ s}^{-1}$ and ε_0 is an adjustable constant. This constant was set as
 188 $2.2 \times 10^{-9} \text{ W kg}^{-1}$ using profiles without ISWs so that the mean ε_{MG} matches the
 189 observed mean dissipation rate. Data within the mixed layer, namely those above the
 190 thermocline ($T > 17.3^\circ\text{C}$), were removed for the comparison. Since ADCP data in the
 191 lower layer have many gaps, only data above the depth of 110 m were used.
 192 Meanwhile, 150-kHZ ADCP data were movingly averaged onto 30-min resolution
 193 before computing shear, as we do not focus on high-frequency shear. Stratification
 194 data were smoothed by an 8-m Bartlett filter to agree with the spatial response of
 195 ADCP. The dissipation rates were vertically averaged over 4-m. Since results
 196 measured by different microstructure instruments may have bias, VMP and Scamp
 197 data were calculated independently. The results are displayed in Figure 4.

198 During VMP measurements, high dissipation values are encountered in strong
 199 sheared and stratified regions (Fig. 4a). The distribution of the measured ε in the space
 200 of N^2 and S^2 is qualitatively more consistent with the M-G parameterization (Fig. 4b),

201 while it is evidently different from the G-H parameterization (Fig. 4c). The
202 distribution pattern of the observed ε in the space of N^2 and S^2 during Scamp
203 measurement is also better reproduced by the M-G parameterization (Figs. 3d to 3f).
204 However, in the regions of $7 \times 10^{-5} \text{s}^{-2} < N^2 < 3 \times 10^{-4} \text{s}^{-2}$, the observed ε are evidently
205 larger than those predicted by the parameterization. This may be associated with
206 nonlinear waves, whose mixing cannot be described by the above two
207 parameterizations [Mackinnon and Gregg, 2003]. Note that most of ISWs appear
208 during Scamp measurements (see Fig. 3). In addition, Ri is partly found to be
209 between 0.25 and 1, but no evident correlation between this parameter and dissipation
210 rate is identified.

211 To obtain the trend of dissipation rates versus S^2 and N^2 alone, the bin-sorted
212 dissipation rates are averaged along N^2 and S^2 , respectively (Figs. 4g-4j). The two
213 parameterizations show large difference in the trend of dissipation rates versus shear
214 (Figs. 4g and 4i), while the M-G model during VMP measurements successfully
215 reproduces the slope of the observed dissipation rates with increasing S^2 . During
216 Scamp measurements, the M-G model also captures the essential relationship of
217 dissipation rate versus shear, although the dissipation rates are larger for $6 \times 10^{-6} \text{s}^{-2}$
218 $< S^2 < 1 \times 10^{-4} \text{s}^{-2}$ due to the effect of nonlinear waves. Regarding the relationship
219 between dissipation rate and stratification (Figs. 4h and 4j), both models reflect the
220 main variation of dissipation rates with stratification.

221

222 **4. Discussion**

223 In the previous section, we showed that the elevated turbulent mixing in the
224 thermocline mainly resulted from strong low-frequency (IT) shears. These large ITs
225 do not directly cause mixing because of their stability ($Ri > 0.25$), but they are likely to

226 directly promote energy transfers toward smaller scale waves that ultimately become
227 unstable leading to mixing. These conditions are consistent with the simple
228 assumption behind the M-G scaling. As a result, we find that the observed dissipation
229 rate is largely reproduced by the M-G model. The simple assumption behind the M-G
230 scaling is that the large-scale shear providing the environment for scattering and
231 breaking of smaller waves results from a few low-frequency waves (ITs or near-
232 inertial waves) rather than from a steady state background GM spectrum on which the
233 G-H scaling applies. This assumption is generally fulfilled in shallow coastal seas such
234 as New England Shelf [*MacKinnon and Gregg, 2003, 2005*] and the Baltic Sea [*van*
235 *der Lee and Umlauf, 2011*], where dissipations were also well parameterized by the
236 M-G model. Therefore, the M-G scaling is mostly known as a shallow water
237 parameterization. However, our observations in the deep sea that fulfill the M-G
238 assumptions, with an internal wave field dominated by a few vertical modes at the
239 semidiurnal frequency, show that the M-G scaling has a wider range of applications
240 than coastal seas.

241 The large ITs that we observe in the thermocline propagate southward and mostly
242 project on mode-3 and mode-4. It is quite likely that they result from scattering of IT
243 beams generated in the northern slope of BB when beams propagate upward from the
244 deep water and hit the thermocline following the scenario described by G01. In this
245 course, nonlinear steepening of ITs further excites ISWs which are as well observed at
246 the mooring location. Since the frequency of ISWs exceeds the buoyancy frequency
247 except in the thermocline, these waves are trapped in this region where they may
248 further increase local mixing. However because of the limited number of
249 microstructure profiles during ISW's events and the long time interval between two

250 adjacent profiles, it was difficult to give evidence of the impact of ISWs on mixing.
251 Additional data are required for this purpose.

252

253 **Acknowledgments** This work was supported by the French National Research
254 Agency "ANR" in the framework of the EPIGRAM project. The authors acknowledge
255 Theo Gerkema for useful comments on this manuscript.

256

257 **Reference**

258 Gerkema, T. (2001), Internal and interfacial tides: beam scattering and local
259 generation of solitary waves, *J. Mar. Res.* 59 (2), 227–255.

260 Gerkema, T., Lam, F. P. A., Maas, and L. R. M. (2004), Internal tides in the Bay of
261 Biscay: conversion rates and seasonal effects, *Deep-Sea Res.*, 51, 2995– 3008.

262 Gill, A. E. (1982), *Atmosphere–Ocean Dynamics*, Academic Press, 662 pp.

263 Gregg, M. C. (1989), Scaling turbulent dissipation in the thermocline, *J. Geophys.*
264 *Res.*, 94(C7), 9686–9698, doi:10.1029/JC094iC07p09686.

265 Grisouard, N., C. Staquet., and T. Gerkema (2011), Generation of internal solitary
266 waves in a pycnocline by an internal wave beam: a numerical study, *J. Fluid Mech.*
267 676, 491–513.

268 MacKinnon, J. A., and M. C. Gregg (2003), Mixing on the late- summer New
269 England Shelf–Solibores, shear, and stratification, *J. Phys. Oceanogr.*, 33(7), 1476–
270 1492.

271 MacKinnon, J. A., and M. C. Gregg (2005), Spring mixing: Turbulence and internal
272 waves during restratification on the New England Shelf, *J. Phys. Oceanogr.*, 35(12),
273 2425–2443.

274 Mercier, M. J., M. Mathur, L. Gostiaux, T. Gerkema, J. M. Magalhães, J. C. B. Da

275 Silva, and T. Dauxois (2012), Soliton generation by internal tidal beams impinging
276 on a pycnocline: laboratory experiments, *J. Fluid Mech.*, 704, 37-60.

277 New, A. L., and R. D. Pingree (1990), Large-amplitude internal soliton packets in the
278 central Bay of Biscay, *Deep-Sea Res.*, 37A (3), 513-524.

279 New, A. L., and J. C. B. DaSilva (2002), Remote-sensing evidence for the local
280 generation of internal soliton packets in the central Bay of Biscay, *Deep-Sea Res.*,
281 49, 915– 934.

282 Pichon, A., Y. Morel, R. Baraille, and L. S. Quaresma (2011), Internal tide
283 interactions in the Bay of Biscay: observations and modeling. *J. Mar. Sys.*, in press.

284 Pingree, R. D., and A. L. New (1991), Abyssal penetration and bottom reflection of
285 internal tidal energy in the Bay of Biscay, *J. Phys.Oceanogr.*, 21, 28–39.

286 Ruddick, B., A. Anis, and K. Thompson (2000), Maximum likelihood spectral fitting:
287 The Batchelor spectrum, *J. Atmos. Oceanic Technol.*, 17, 1541-1554.

288 Shih, L. H., J. R. Koseff, G. N. Ivey, and J. H. Ferziger (2005), Parameterization of
289 turbulent fluxes and scales using homogenous sheared stably stratified turbulence
290 simulations, *J. Fluid Mech.*, 525, 193–214, doi:10.1017/S0022112004002587.

291 van der Lee, E. M., and L. Umlauf (2011), Internal wave mixing in the Baltic Sea:
292 Near-inertial waves in the absence of tides, *J. Geophys. Res.*, 116, C10016,
293 doi:10.1029/2011JC007072.

294

295

296

297

298

299

300

301 **Captions**

302 **Figure 1:** (a) Map showing bathymetry in the BB and the observation site (the black
303 point). The slash line indicates the possible propagation path of the seaward traveling
304 internal tidal beams generated on the northern slope. Their characteristic path is given
305 in the inserted panel (blue line with arrows). The red curve is typical model
306 topography in the BB along the cross-slope direction. The vertical line indicates the
307 observation location. (b) Profile of $N(z)$: The vertical line indicates a frequency of
308 $1/25 \text{ min}^{-1}$. Vertical structures of displacement $\Phi(z)$ for the mode-1 (blue), mode-2
309 (green), mode-3 (red) and mode-4 (pink) waves with (c) semidiurnal and (d) $1/25 \text{ min}^{-1}$
310 1 frequencies. In (c), the black solid line is the measured IT displacement profile
311 around 3h/19th (black solid line). The dashed line is sum of projected mode-3 and
312 mode-4. (e) Observed velocity profiles (red and blue lines) during two ISWs (marked
313 by arrows in Figure 3a) in a semi-Lagrangian frame and velocity profiles of IT mode-
314 4 (black dashed line) and trapped mode-1 (black solid line). Note that both
315 displacements and velocities have been normalized.

316 **Figure 2:** (a) Temperature. White vertical lines indicate the times of CTD profiles. (b)
317 Current Velocity amplitude. Time series of meridional velocities obtained from (c)
318 150-kHZ and (d) 38-kHZ ADCPs. Data in (d) have been movingly averaged to 10-
319 min resolution. Two black lines in (c) are isotherms of 17.3°C and 12.9°C, indicating
320 depths of the thermocline, similar for Figures 3b to 3e (white lines in Figures 3d and
321 3e).

322 **Figure 3:** (a) Velocity amplitudes during VMP/Scamp observation. The arrows
323 indicate ISWs plotted in Figure 2b. (b) Dissipation rate. (c) Diacycnal diffusivity.
324 Isotherms whose interval is 0.5°C (white lines) are over-plotted on (b) and (c). (d) N^2 .

325 (e) $(S_4)^2$. A 4-m running average is used for (b) and (c). Data in (e) have 30-min
 326 resolution. The embodied panels in (b), (c) and (d) is time-averaged ε , K_p and N^2 (blue)
 327 and $(S_4)^2$ (red) along the isotherms
 328 **Figure 4:** Distribution of dissipation rates in bins of N^2 and S^2 from observations (a
 329 and d) and the M-G (b and e) and G-H (c and f) parameterizations. The averaged
 330 dissipation rate in bins of S^2 (g and i) and N^2 (h and j), respectively. (a), (b), (c), (g)
 331 and (h) for the observation period of VMP. (d), (e), (f), (i) and (j) for the observation
 332 period of Scamp. The red, blue and green curves in the latter 4 panels are the results
 333 of the observation, M-G model and G-H model, respectively. The grey shading
 334 indicates 95% confidence interval. The oblique solid and dashed lines in (a) to (f) are
 335 the boundaries of $Ri=0.25$ and $Ri=1$.

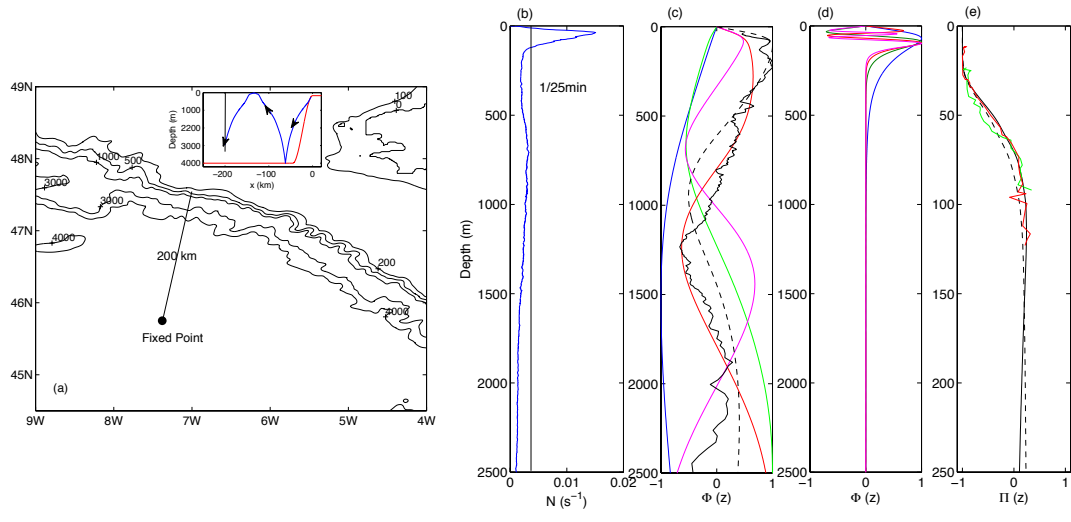


Figure 1

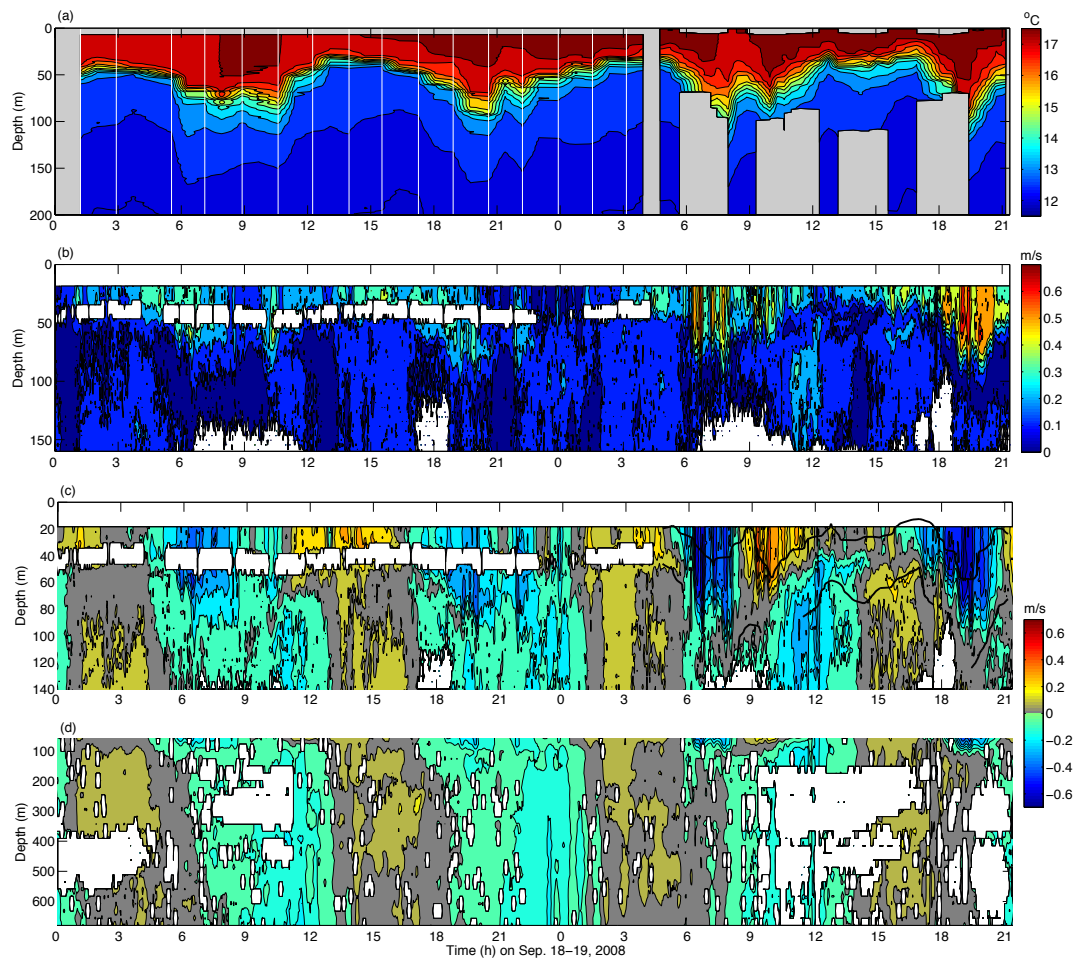


Figure 2

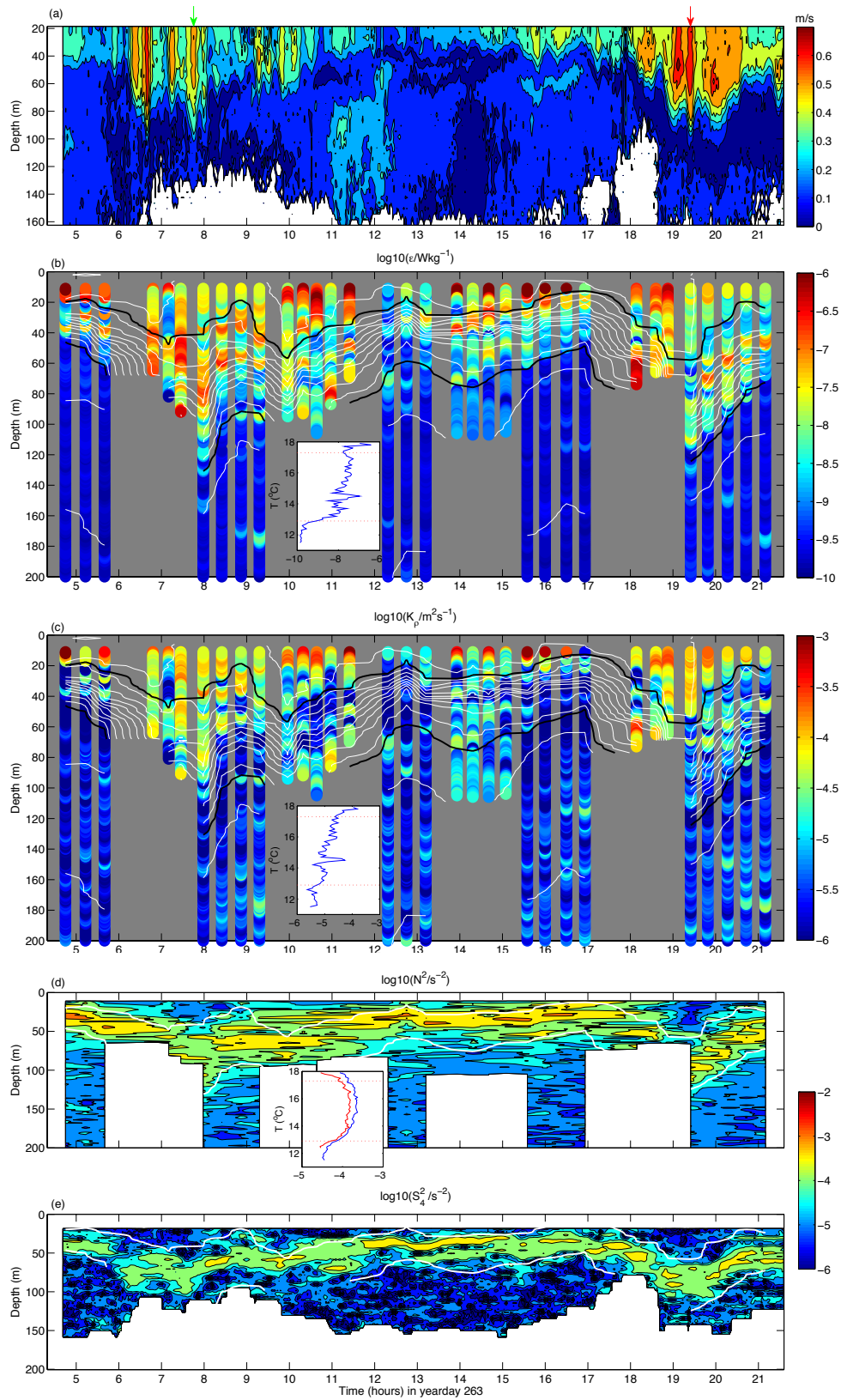


Figure 3

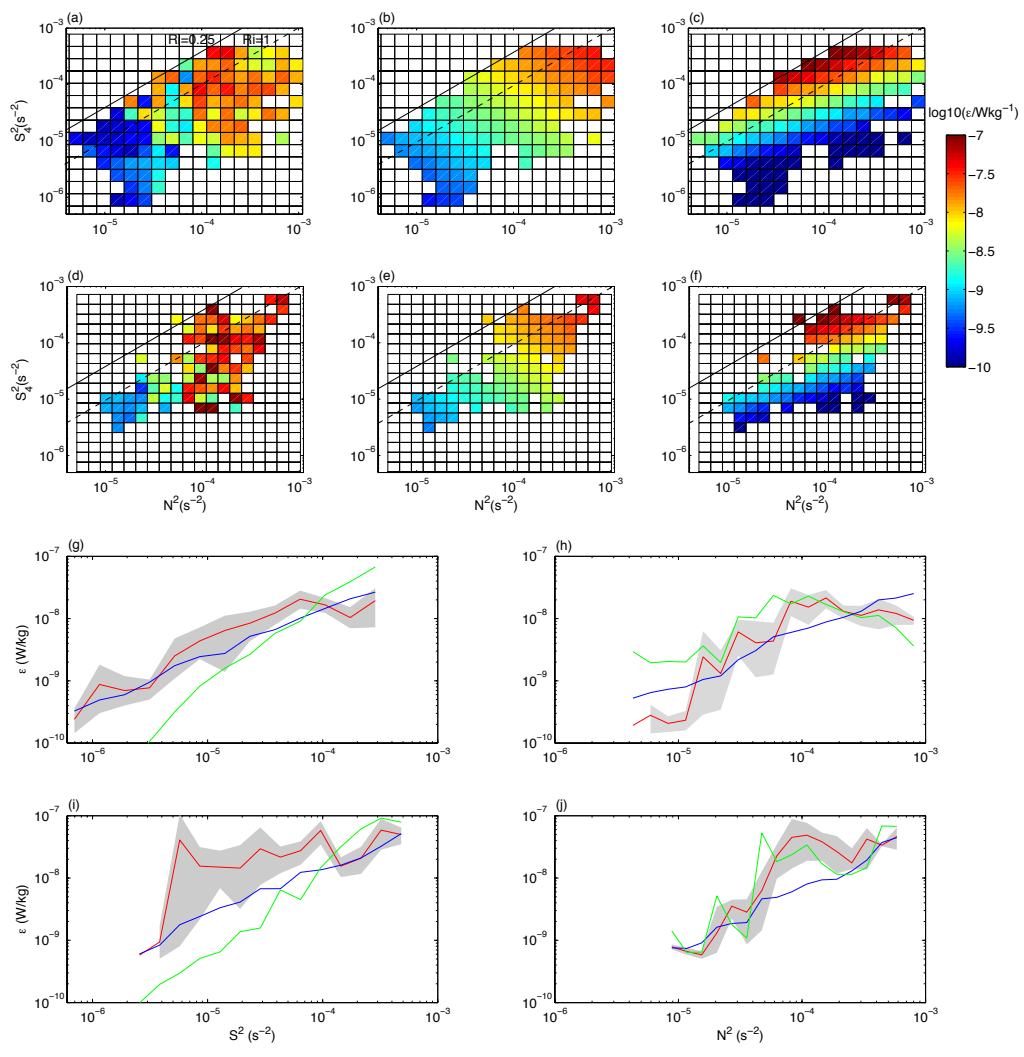


Figure 4